A New Approach for Accurate Prediction of Subharmonic Oscillation in Switching Regulators–Part II: Case Studies

A. El Aroudi, *Senior Member, IEEE*

***Abstract*—This part of the paper illustrates the use of the expression derived in Part I for predicting subharmonic oscillation in switching regulators. Six case studies with different control schemes from the recent literature are used to validate the novel approach and the new derived expression which is benchmarked for these case studies against results obtained using the discrete-time modeling approach or Floquet theory combined with Filippov method. Numerical simulations from the circuit-level switched models, implemented in PSIM© software, are used to demonstrate the correctness of the derived closed-form condition. A procedure is presented to apply the approach of the paper to power converters with nonlinear sources such as photovoltaic (PV) arrays or fuel cells. Experimental measurements from a boost converter prototype for PV applications are also provided to validate the theoretical predictions and the numerical simulations showing a remarkable agreement.**

***Index Terms*—Circuit stability, DC-DC power conversion, Bifurcation, Bilinear systems, Nonlinear systems, Power electronics, Switched mode power supplies, Time domain analysis.**

I. Introduction

SEVERAL methods for predicting subharmonic oscillation in switching power converters are present in the literature. Part I [1] classified and summarized the main approaches, presented a novel one and established a new analytical expression for accurate prediction of this phenomenon under fixed frequency Pulse width Modulation (PWM) and Continuous Conduction Mode (CCM) operation. This part of the paper complements Part I and illustrates the usefulness of the new derived expression. Both simulation and experimental results are presented to validate the novel approach using different examples of switching converters. The main findings detailed in Part I will be first summarized for easy reference.

Consider a switching regulator working in CCM that can be described by a piecewise linear as follows:

$$\dot{\mathbf{x}} = \mathbf{A}_1\mathbf{x}+\mathbf{B}_1\mathbf{w}, \quad \text{for} \quad u=1, \tag{1a}$$

$$\dot{\mathbf{x}} = \mathbf{A}_0\mathbf{x}+\mathbf{B}_0\mathbf{w}, \quad \text{for} \quad u=0, \tag{1b}$$

$$\dot{x}_i = e. \tag{1c}$$

A. El Aroudi is with the GAEI research center, Departament d'Enginyeria Electrònica, Elèctrica i Automàtica, Escola Tècnica Superior d'Enginyeria, Universitat Rovira i Virgili, 43007, Tarragona, Spain (e-mail:abdelali.elaroudi@urv.cat).

This work was supported by the Spanish *Ministerio de Economía y Competitividad* under grants DPI2013-47437-R.

Copyright© 2016 IEEE. Personal use of this material is permitted. However, permission to use this material for any other purposes must be obtained from the IEEE by sending an email to pubs-permissions@ieee.org.

Color versions of one or more of the figures in this paper are available online at http://ieeexplore.ieee.org

where u is the square wave signal generated by the PWM process which is applied to the main switch S. $\mathbf{A}_0 \in \mathbb{R}^{n\times n}$, $\mathbf{A}_1 \in \mathbb{R}^{n\times n}$, $\mathbf{B}_0 \in \mathbb{R}^{n\times p}$ and $\mathbf{B}_1 \in \mathbb{R}^{n\times p}$ are the system state matrices and $\mathbf{w} \in \mathbb{R}^p$ is the vector of the external parameters of the plant and/or the controller supposed to be constant within a switching cycle. Recall that (1a)-(1c) includes the dynamics of both the power stage and the controller. The variable x_i in (1c) stands for the integral of the sensed outer error e in both Voltage Mode Control (VMC) and Current Mode Control (CMC) strategies. Note that this variable was deliberately separated from the rest of state variables to start with a *well-posed* problem as was detailed in Part I where it was demonstrated that at the boundary of subharmonic oscillation the following equality holds:

$$-\mathbf{K}^\intercal(\mathbf{I}+\mathbf{\Phi})^{-1}\mathbf{\Phi}_1(\mathbf{m}_1(\mathbf{x}(0))+\mathbf{m}_0(\mathbf{x}(0)))+W_i e(DT) = m_a. \tag{2}$$

where m_a is the slope of the external ramp signal used either for modulation or for stabilization, $\mathbf{K}$ is the vector of feedback coefficients and W_i is the integral gain. For stability, the ramp slope m_a must be greater than a certain critical value given by the left side of (2). In control strategies where a ramp signal is not used ($m_a = 0$), the left hand side of (2) must be negative for the system to be stable. The vectors $\mathbf{m}_1(\mathbf{x}) = \mathbf{A}_1\mathbf{x}+\mathbf{B}_1\mathbf{w}$ and $\mathbf{m}_0(\mathbf{x}) = \mathbf{A}_0\mathbf{x}+\mathbf{B}_0\mathbf{w}$ are the vector fields for each linear configurations of the converter. The matrices $\mathbf{\Phi}_1 = e^{\mathbf{A}_1 DT}$ are $\mathbf{\Phi}_0 = e^{\mathbf{A}_0(1-D)T}$ are the state transition matrices evaluated at their corresponding time intervals and $\mathbf{\Phi} = \mathbf{\Phi}_1\mathbf{\Phi}_0$. The variable D is the steady-state duty cycle and $\mathbf{x}(0)$ is the steady-state periodic orbit evaluated at the start of the switching period and which can be expressed by:

$$\mathbf{x}(0) = (\mathbf{I}-\overline{\mathbf{\Phi}})^{-1}\overline{\mathbf{\Psi}}, \tag{3}$$

where $\overline{\mathbf{\Phi}} = \mathbf{\Phi}_0\mathbf{\Phi}_1$ and $\overline{\mathbf{\Psi}} = \mathbf{\Phi}_0\mathbf{\Psi}_1 + \mathbf{\Psi}_0$, $\mathbf{\Psi}_1 = \mathbf{A}_1^{-1}(\mathbf{\Phi}_1 - \mathbf{I})\mathbf{B}_0\mathbf{w}$ and $\mathbf{\Psi}_0 = \mathbf{A}_0^{-1}(\mathbf{\Phi}_0 - \mathbf{I})\mathbf{B}_0\mathbf{w}$. Similarly, one can obtain that $\mathbf{x}(DT)$, the value of the periodic orbit at the switching instant DT within the switching period is as follows:

$$\mathbf{x}(DT) = (\mathbf{I}-\mathbf{\Phi})^{-1}\mathbf{\Psi}, \tag{4}$$

where $\mathbf{\Psi} = \mathbf{\Phi}_1\mathbf{\Psi}_0 + \mathbf{\Psi}_1$. Expression (2) can help switching converter designers to determine the safe region in the parameter space where the system operates at a desired periodic regime. It should also be noted that although the focus of this work is on subharmonic oscillation boundary, (2) can be easily adjusted to predict another instability boundary known as saddle-node bifurcation [2]. Namely, this phenomenon can

also be detected using (2) by changing the sum $\mathbf{m}_1(\mathbf{x}(0)) + \mathbf{m}_0(\mathbf{x}(0))$ by the difference $\mathbf{m}_1(\mathbf{x}(0)) - \mathbf{m}_0(\mathbf{x}(0))$ and the sum $\mathbf{I} + \mathbf{\Phi}$ by the difference $\mathbf{I} - \mathbf{\Phi}$. More information can be found in [3]. The slow scale instability that in most of the cases can be predicted analytically by using simple averaging procedures such as in [4] is omitted in this work.

To illustrate the application of the new approach introduced in Part I and to validate the closed-form expression in (2), it is benchmarked in this paper for six different case studies against results from discrete-time modeling or Floquet theory combined with Filippov method. Several key parameters which affect the system dynamical behavior are chosen to show the subharmonic oscillation boundaries which are presented in suitable two-dimensional and three-dimensional parameter spaces.

Numerical simulations from the circuit-level switched model of the considered examples implemented in PSIM© software are also performed to demonstrate the validity and the correctness of the derived closed-form condition. For switching converters with a nonlinear source such as a fuel cell or a PV generator, a linearization approach is presented to readily apply the results of this paper. The approach is then applied to a PV-fed boost converter working at the maximum power point (MPP) of the PV generator obtaining a remarkable agreement among the theoretical findings, the numerical simulations and the experimental measurements.

The rest of the paper is organized as follows. Section II illustrates the use of the new derived expression for two switching regulators from the recent literature with first-order power stages. Subsequently, other examples are used in Section III to validate the new obtained expression for high-order switching regulators with both linear and bilinear power stages. An additional example for PV applications with experimental validation is considered in Section IV. Finally, some concluding remarks are summarized in the last section.

II. Switching regulators with first-order power stage

A. Example 1: A boost converter under Current Mode Control (CMC) and a Proportional-Integral (PI) compensator [5]

Consider a first-order boost converter with a constant output voltage representing a battery or a regulated dc bus and take into account parasitic parameters of the inductor and the switching devices [5]. The circuit diagram and the parameter values are shown in Fig. 1. The system is under CMC with a PI controller to regulate the inductor current. The only power stage state variable is the inductor current i_L which is governed by the following differential equation:

$$\frac{\mathrm{d}i_L}{\mathrm{d}t} = \frac{1}{L}(-(r_1 u + r_0(1-u))i_L + v_g - V_{\mathrm{S}} u - (v_o + V_{\overline{\mathrm{S}}})(1-u)). \tag{5}$$

where $r_1 = r_L + r_s + r_{\mathrm{S}}$ and $r_0 = r_L + r_s + r_{\overline{\mathrm{S}}}$. All the parameters can be identified in Fig. 1. In particular, $r_{\overline{\mathrm{S}}}$, r_S, $V_{\overline{\mathrm{S}}}$ and V_{S} are the diode and the switch (IGBT) turn-on resistances and voltages respectively and r_s is a small shunt resistance used in practice to sense the inductor current. The voltage across r_s is amplified by a voltage amplifier with gain N, hence the total current gain is the product $R_s = N r_s$. In our case, $r_s = 0.01\ \Omega$ is used to convert inductor current to a voltage which is amplified by a factor $N = 100$ and hence $R_s = 1\ \Omega$. The error between this voltage and a suitable reference $v_r = R_s i_{\mathrm{ref}}$ is processed using an error amplifier in the form of a PI network using the passive components R_i and C_i. The control signal v_{con} is the output of the PI controller and can be expressed as follows:

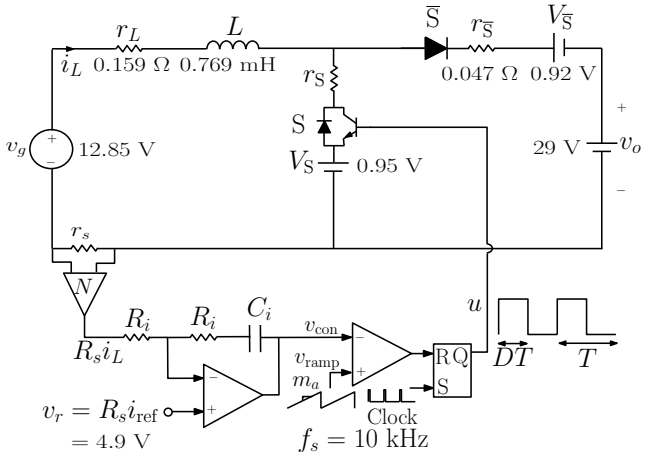


Fig. 1. A boost converter under a Proportional-Integral (PI) Current Mode Control (CMC) scheme [5].

$$v_{\mathrm{con}}(t) = v_r - R_s i_L(t) + W_i \int (v_r - R_s i_L(t))\mathrm{d}t, \tag{6}$$

Accordingly, the proportional current gain is $k_i = R_s = 1\ \Omega$ as in [5]. The integral gain $W_i = 1/(R_i C_i)$ is considered as a design parameter and can be varied by varying the capacitance C_i. For this system one can see from (5) that[1]:

$$\mathbf{A}_1 = -\frac{r_1}{L}\ ,\ \mathbf{A}_0 = -\frac{r_0}{L}\ ,\mathbf{B}_1 = \begin{pmatrix} \frac{1}{L} \\ 0 \end{pmatrix}^{\intercal}, \tag{7a}$$

$$\mathbf{B}_0 = \begin{pmatrix} 0 \\ \frac{1}{L} \end{pmatrix}^{\intercal},\ \mathbf{w} = \begin{pmatrix} v_g - V_{\overline{\mathrm{S}}} \\ v_g - (v_o + V_{\mathrm{S}}) \end{pmatrix}. \tag{7b}$$

Let $a_1 = \mathbf{A}_1 T = -r_1 T/L$, $a_0 = \mathbf{A}_0 T = -r_0 T/L$, $b_1 = \mathbf{B}_1 \mathbf{w} = (v_g - V_{\overline{\mathrm{S}}})/L$ and $b_0 = \mathbf{B}_0 \mathbf{w} = (v_g - (v_o + V_{\mathrm{S}}))/L$. Therefore, the subharmonic oscillation condition in (2) can be particularized for this example as follows:

$$-R_s \frac{((\mathbf{A}_1 + \mathbf{A}_0) i_L(0) + b_1 + b_0)}{1 + e^{a_1 D + a_0 (1-D)}} e^{a_1 D} - R_s W_i \Delta i_L = m_a, \tag{8}$$

where $\Delta i_L := i_L(DT) - i_{\mathrm{ref}}$ is the inductor current ripple amplitude in the $T-$periodic regime and $i_L(0)$ and $i_L(DT)$

[1]Although this is a first-order power stage and its state-space model is first-order, its corresponding parameters $\mathbf{A}_1$ and $\mathbf{A}_0$ are represented in boldfaced upper case to be consistent with all the rest of the paper.

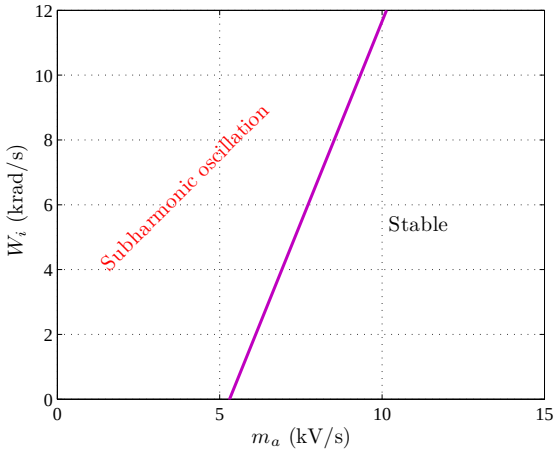


Fig. 2. Subharmonic oscillation limit in terms of the ramp slope m_a and the integral gain W_i for a boost converter under CMC with a PI control [5].

are its peak and valley values given by:

$$i_L(0) = \frac{(e^{a_1 D+a_0(1-D)} - e^{a_0(1-D)})b_1}{a_1 T(1-e^{a_1 D+a_0(1-D)})} + \frac{(e^{a_0(1-D)}-1)b_0}{a_0 T(1-e^{a_1 D+a_0(1-D)})}, \quad (9a)$$

$$i_L(DT) = \frac{(e^{a_1 D+a_0(1-D)} - e^{a_1 D})b_0}{a_0 T(1-e^{a_1 D+a_0(1-D)})} + \frac{(e^{a_1 D}-1)b_1}{a_1 T(1-e^{a_1 D+a_0(1-D)})}, \quad (9b)$$

In this example, the current reference $i_{\rm ref} = v_r/R_s$ (also the average inductor current) is related to the steady-state duty cycle D by the following constraint which can be obtained by performing a net volt-second balance in steady-state [6]:

$$D = \frac{v_o + V_{\overline{\rm S}} + r_0 i_{\rm ref} - v_g}{v_o + V_{\overline{\rm S}} + (r_{\overline{\rm S}} - r_{\rm S})i_{\rm ref} - V_{\rm S}}. \quad (10)$$

The parameter values used, shown in Fig. 1, are the same ones of [5]. Accordingly, the steady-state operating duty cycle is $D = 0.6554$. In [5], the stability boundary in terms of the ramp slope m_a and the integral gain W_i was obtained by tracking the movement of the eigenvalues of the exact discrete-time model and an improved averaged model. The results were also validated experimentally. Here, the expression of the critical W_i is explicitly derived in terms of all system parameters. According to (8), the critical integral gain at the boundary of subharmonic oscillation can be expressed as follows:

$$W_i = \frac{m_a}{R_s \Delta i_L} + \frac{(\mathbf{A}_1 + \mathbf{A}_0)T i_L(0) + b_1 + b_0}{R_s \Delta i_L (1 + e^{a_1 D+a_0(1-D)})} e^{a_1 D}, \quad (11)$$

Note that for a fixed value of the steady-state duty cycle D, the critical value of the integral gain W_i is a linear function of m_a with a slope $1/(R_s \Delta i_L)$. Moreover, the larger the ripple is, the smaller the critical value of W_i is. Note also that for a fixed value of the steady-state duty cycle D, the minimal external ramp slope required for stabilization increases when the integral gain W_i is increased. Fig. 2 shows the critical integrator gain W_i in terms of the external ramp slope m_a using (11). A remarkable agreement can be observed by comparing Fig. 2 here and Fig. 12 in [5] which was also validated experimentally in the same paper. However, while using the two approaches described in [5] could result in a high computational load, the critical integral gain W_i is explicitly given by (11) and the corresponding plot in terms of any parameter requires much less computational effort.

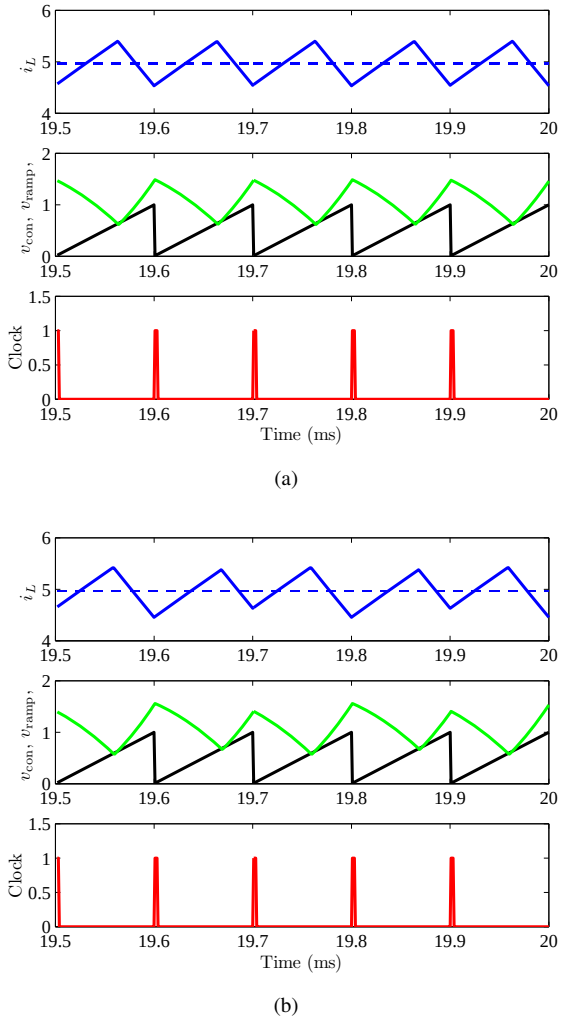


Fig. 3. Waveforms of the boost converter of Example 1. (a) $W_i = 11.5$ krad/s, before and (b) $W_i = 11.7$ krad/s, after exhibiting subharmonic oscillation.

Numerical simulations using PSIM© were performed to check the dynamics of the system in both sides of the boundary. Fig. 3 shows the waveforms of the inductor current, the control voltage $v_{\rm con}$ and the ramp signal $v_{\rm ramp}$ just before and just after subharmonic oscillation takes place for $V_M = 1$ V, i.e., $m_a = 10$ kV/s. Let $W_i = 11.5$ krad/s, the converter is stable as predicted in Fig. 2 and confirmed by numerical simulations depicted in Fig. 3(a) obtained from the switched circuit-level model. Let $W_i = 11.7$ krad/s, the converter exhibits subharmonic oscillation as predicted in Fig. 2 and confirmed by the simulations shown in Fig. 3(b).

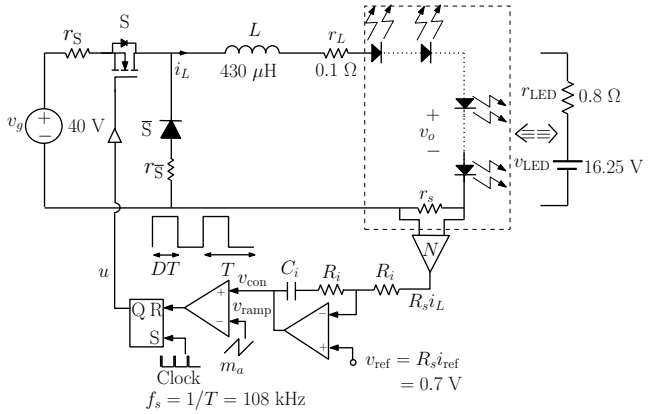


Fig. 4. Circuit diagram of the buck LED driver of Example 2 [7], [8].

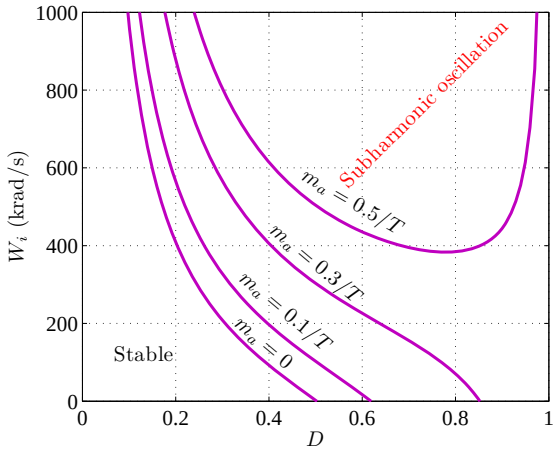


Fig. 5. Subharmonic oscillation boundary of a buck LED driver under CMC and PI controller in terms of the steady-state duty cycle D and the integral gain W_i for different values of the compensating ramp slope m_a.

B. Example 2: A buck LED driver under CMC with a PI controller [7], [8]

In this second illustrative example, we consider a buck LED driver depicted in Fig. 4 with the parameter values shown in the same figure which are the same ones as those in [7], [8]. These parameters correspond to pure white LEDs, Z-POWER w42182 [8]. The system is under CMC with a PI controller. Note that in this particular topology, the inductor current coincides with the LED current. Hence, buck converters do not need an output capacitor when they work as LED drivers because the output LED current is continuous for this topology which is therefore widely used as an LED driver due to its simplicity, low cost and fast response. Therefore, CMC without a voltage loop is a natural way for controlling buck LED drivers like in [7], [8]. A small resistance $r_s = 0.01$ Ω is used to convert the LED current to a voltage which is amplified by a factor $N = 100$ to obtain a voltage equal in magnitude to the LED current. Like in Example 1, the error between this voltage and its reference is processed by a PI controller to provide the control voltage $v_{\rm con}$ which is finally compared with the ramp signal $v_{\rm ramp}$ to decide the duty cycle of the LED driver. Let $r_1 = r_{\rm LED} + r_L + r_s + r_{\rm S}$ and $r_0 = r_{\rm LED} + r_L + r_s + r_{\overline{\rm S}}$. The only power stage state variable is the inductor current i_L which is governed by the following differential equation:

$$\frac{{\rm d}i_L}{{\rm d}t} = -(\frac{r_1}{L}u + \frac{r_0}{L}(1-u))i_L - \frac{v_{\rm LED}}{L} + \frac{v_g}{L}u, \qquad (12)$$

For this system one has that:

$$\mathbf{A}_1 = -\frac{r_1}{L}\ ,\ \mathbf{A}_0 = -\frac{r_0}{L}\ ,\mathbf{B}_1 = \begin{pmatrix} \frac{1}{L} \\ -\frac{1}{L} \end{pmatrix}^{\mathsf{T}}, \qquad (13a)$$

$$\mathbf{B}_0 = \begin{pmatrix} 0 \\ -\frac{1}{L} \end{pmatrix}^{\mathsf{T}}, \mathbf{w} = \begin{pmatrix} v_g \\ v_{\rm LED} \end{pmatrix}. \qquad (13b)$$

In [7], [8], the root locus analysis was applied to the discrete-time model of the converter to locate the stability boundary and experimental results were presented to confirm the design. Subharmonic oscillation was observed but no condition for its occurrence was derived. To use the same parameter values considered in [7], [8], let us consider $r_{\rm S} = r_{\overline{\rm S}} = 0$, hence $r_1 = r_0 = r_{\rm LED} + r_L + r_s := r$ and $\mathbf{A}_1 = \mathbf{A}_0 = -r/L$. Let $a = \mathbf{A}_1 T = \mathbf{A}_0 T = -rT/L$, $b_1 = \mathbf{B}_1\mathbf{w} = (v_g - v_{\rm LED})/L$ and $b_0 = \mathbf{B}_0\mathbf{w} = -v_{\rm LED}/L$. Hence, the subharmonic oscillation condition in (2) becomes as follows:

$$-R_s\frac{(2\mathbf{A}i_L(0) + b_1 + b_0)}{1+e^{aD}}e^a + R_s W_i(i_{\rm ref} - i_L(DT)) = m_a, \qquad (14)$$

where $i_L(0)$ and $i_L(DT)$ are given by:

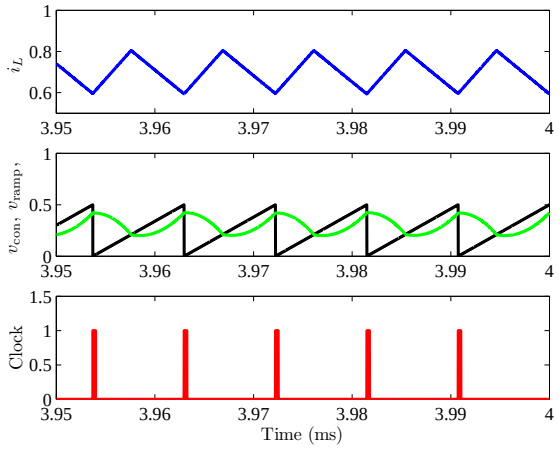
$$i_L(0) = \frac{(e^{aD} - e^{a(1-D)})b_1}{aT(1-e^{aD})} + \frac{(e^{a(1-D)}-1)b_0}{aT(1-e^{aD})}, \qquad (15a)$$

$$i_L(DT) = \frac{(e^{a} - e^{aD})b_0}{aT(1-e^{aD})} + \frac{(e^{aD}-1)b_1}{aT(1-e^{aD})}. \qquad (15b)$$

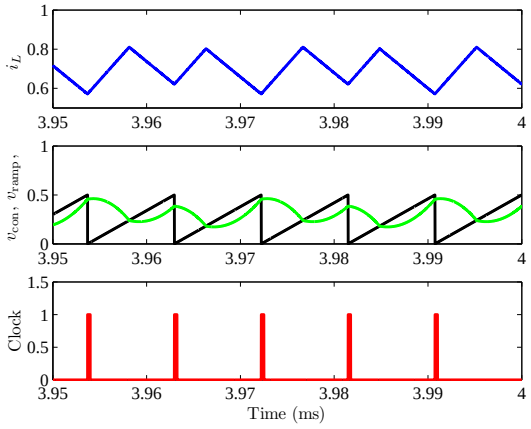
For this example, the current reference $i_{\rm ref}$ (also the steady-state average LED current) is related to the steady-state duty cycle D by the following expression which is obtained by performing a net volt-second balance in steady-state regime:

$$D = \frac{ri_{\rm ref} + v_{\rm LED}}{v_g} \Rightarrow i_{\rm ref} = \frac{v_g D - v_{\rm LED}}{r}. \qquad (16)$$

The stability boundary is shown in Fig. 5 for different values of the ramp slope m_a. Note that the range of steady-state duty cycles D guaranteing stability becomes smaller as W_i increases and that the bigger W_i is, the bigger the ramp slope needed for stabilization is for a fixed value of D. Numerical simulations, using the circuit-level switched model implemented in PSIM©, were performed to check the dynamics of the system in both sides of the boundary. Let $m_a = 0.5/T = 54$ kV/s. If $W_i = 555$ krad/s, the converter is stable as predicted in Fig. 5 and confirmed by numerical simulations depicted in Fig. 6(a). If $W_i = 565$ krad/s, the converter exhibits subharmonic oscillation as predicted in Fig. 5 and confirmed by the simulations shown in Fig. 6(b).



(a)



(b)

Fig. 6. Waveforms of the buck LED driver of Example 2. (a) $W_i = 555$ krad/s, before and (b) $W_i = 565$ krad/s, after exhibiting subharmonic oscillation. $m_a = 54$ kV/s.

III. High-order switching converters with linear and bilinear power stage

A. Example 3: A buck converter under VMC and a PI controller [9], [10]

The system that will be considered in this example is a very known and widely studied buck converter under VMC with a PI controller [9][2]. The schematic circuit diagram as well as the fixed parameter values are shown in Fig. 7. The vector of the state variables of the power stage is $\mathbf{x} = (v, i_L)^\intercal$, where v is the output capacitor voltage and i_L is the inductor current. The system state equations are as follows:

$$\frac{\mathrm{d}v}{\mathrm{d}t} = -\frac{v}{RC} + \frac{i_L}{C}, \tag{17a}$$

$$\frac{\mathrm{d}i_L}{\mathrm{d}t} = -\frac{v}{L} + \frac{v_g}{L}u, \tag{17b}$$

[2]In [10], [12]–[16] the same parameter values are considered but only a proportional controller was used.

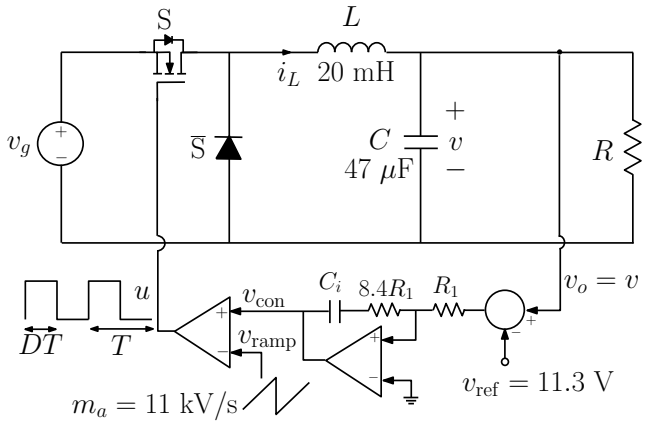


Fig. 7. The buck converter under VMC of Example 3.

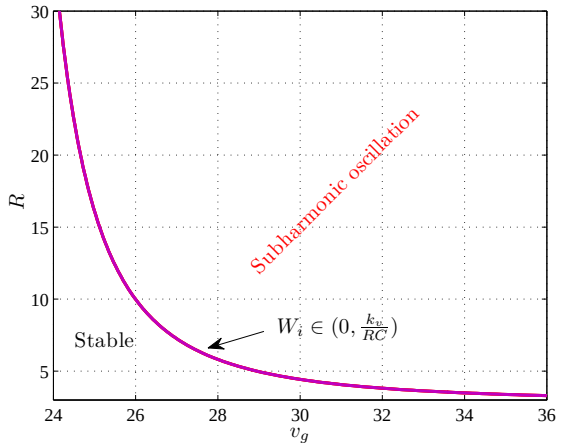


Fig. 8. Subharmonic oscillation boundary in terms of the input voltage v_g and the load resistance R for a buck converter under VMC with a PI controller for $W_i \in (0, k_v/(RC))$.

Accordingly, the only external input parameter to the power stage is $\mathbf{w} = v_g$ and the system state-space matrices are:

$$\mathbf{A}_1 = \mathbf{A}_0 = \begin{pmatrix} -\frac{1}{RC} & \frac{1}{C} \\ -\frac{1}{L} & 0 \end{pmatrix}, \mathbf{B}_1 = \begin{pmatrix} 0 \\ \frac{1}{L} \end{pmatrix}, \tag{18a}$$

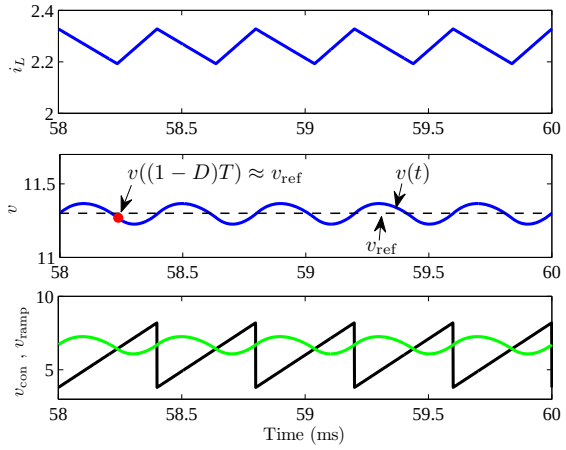
$$\mathbf{B}_0 = \begin{pmatrix} 0 \\ 0 \end{pmatrix}, \mathbf{K} = \begin{pmatrix} k_v \\ 0 \end{pmatrix}. \tag{18b}$$

For this example, the voltage reference $v_{\rm ref}$ (also the steady-state average output voltage) is related to the steady-state duty cycle D and the input voltage by the constraint $D = v_{\rm ref}/v_g$. In [9], [10] the stability boundary is plotted in terms of the input voltage v_g and the load resistance R (see Fig. 6 in [10] and Fig. 7 in [9]). The results were obtained from Floquet theory by checking when one of the eigenvalue of the monodromy matrix becomes -1 and were also validated experimentally. For ease of comparison, the same diagram is plotted here by using (2). The result is shown in Fig. 8. It can be observed that when, for example, $R = 22\ \Omega$, the critical value of v_g for subharmonic oscillation occurrence is very close to 24.5 V in a perfect agreement with [9], [10], [16].

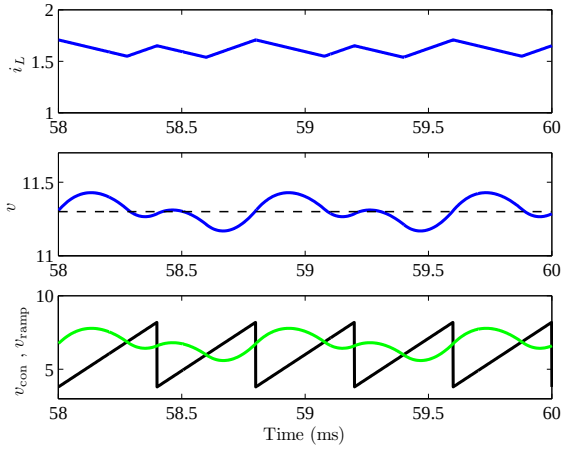
It should be noted that this example uses an LEM strategy and a change of variable $D \rightarrow (1-D)$ must be done in (2) together with a sign inversion in the voltage feedback gain k_v. It is also worth noting that in a second-order (or higher) switching converter under a feedback loop involving an integral action, a slow scale instability (also called Hopf bifurcation) could take place before subharmonic oscillation occurs. Based on an approximated averaging procedure [11], it can be demonstrated that the Hopf bifurcation can be avoided in a buck converter under VMC with a PI controller if the integral gain W_i fulfills the following condition:

$$W_i < \frac{V_M + k_v v_g}{RCv_g} := W_{i,\text{slow}}. \tag{19}$$

If $V_M \ll k_v v_g$, which is the case in practice, the critical value of the integral gain for avoiding the slow scale instability can be approximated by $W_{i,\text{slow}} \approx k_v/(RC)$. In order to check the dependence of the subharmonic oscillation on the integral gain W_i, its boundary is plotted for different values of this parameter in the range $(0, k_v/(RC)$ obtaining practically the same curve for all this range. The parameter W_i was maintained less than $k_v/(RC)$ to avoid slow scale instability [11]. The fact that the subharmonic oscillation curve is practically the same for all the considered values of W_i confirms the conjecture in [9] which states that the parameter W_i has practically no effect on this phenomenon. This also confirms the conclusion in [17] where it was stated that the subharmonic oscillation boundary is practically unaffected by the integrator time constant of the voltage loop PI controller. This happens because the error voltage evaluated at the switching instant $e((1-D)T) := v((1-D)T) - v_{\text{ref}}$ is practically zero as it was mentioned in Part I. For this reason, it is not expected to see a significant change in the subharmonic oscillation boundary if the integral variable had been ignored in the switching decision. Numerical simulations using PSIM© were performed to check the dynamics of the system in both sides of the boundary. Let $v_g = 28$ V. According to Fig. 8, the critical value of the load resistance for losing the stability is $R = 5.815\ \Omega$. Let $R = 5\ \Omega$, the converter is stable as predicted in Fig. 8 and confirmed by numerical simulations depicted in Fig. 9(a), where it can also be observed that $v((1-D)T) \approx v_{\text{ref}}$. Let $R = 7\ \Omega$, the converter exhibits subharmonic oscillation as predicted in Fig. 8 and confirmed by the simulations shown in Fig. 9(b). In the previous time-domain simulations, the time constant of the integrator was fixed at $\tau_i = 6$ ms by selecting $C_i = 222$ nF and $R_1 = 89.37$ MΩ implying that $k_v = 8.4$ and $W_i = k_v/\tau_i = 8.4/0.006 = 1.4$ krad/s which is smaller than $W_{i,\text{slow}} \approx k_v/(RC) = 16.21$ krad/s. The same *steady-state* behavior will be obtained for all values of $W_i < W_{i,\text{slow}}$.



(a) $R = 5\ \Omega$.



(b) $R = 7\ \Omega$.

Fig. 9. Waveforms of the buck converter under a PI VMC of Example 3. (a) $R = 5\ \Omega$, before and (b) $R = 7\ \Omega$, after exhibiting subharmonic oscillation. v_g= 28 V, $W_i = 1.4$ krad/s.

B. Example 4: A buck converter under V^{2}I$_C$ control with an ESR and an ESL in the output capacitor [18]

V^{2}I$_C$ control is a ripple-based strategy that presents a very fast response in front of load and voltage reference step changes. It is composed by a slow loop, where the output voltage is regulated with a linear PI controller, and a fast loop, where the error of the output voltage and the current through the output capacitor are added to the compensating ramp. Using the capacitor current in the feedback loop can be viewed as mean to insert the derivative action in the voltage loop while avoiding noise injection [19]. Fig. 10 shows the circuit diagram of a buck converter under a V^{2}I$_C$ control. Excluding the integral variable x_i, the vector of the state variables is $\mathbf{x} = (v, v_s, i_L, i_C, i_s)^\intercal$. Let $R_1 = r_{\text{on1}} + r_L + R$ and $R_2 = r_{\text{on2}} + r_L + R$. By applying KVL to the circuit diagram, the following state equations are obtained:

$$\frac{\mathrm{d}v}{\mathrm{d}t} = \frac{i_C}{C}, \tag{20a}$$

$$\frac{\mathrm{d}v_s}{\mathrm{d}t} = \frac{i_s}{C_s}, \tag{20b}$$

$$\frac{\mathrm{d}i_L}{\mathrm{d}t} = -\frac{R_1 i_L + v_g}{L}u - \frac{R_2 i_L}{L}(1-u) + \frac{R}{L}(i_C + i_s + i_o), \tag{20c}$$

$$\frac{\mathrm{d}i_C}{\mathrm{d}t} = -\frac{v_C}{\ell_C} + \frac{R}{\ell_C}i_L - \frac{R + r_C}{\ell_C}i_C - \frac{R}{\ell_C}i_s - \frac{R}{\ell_C}i_o, \tag{20d}$$

$$\frac{\mathrm{d}i_s}{\mathrm{d}t} = -\frac{v_s}{\ell_s} + \frac{R}{\ell_s}i_L - \frac{R}{\ell_s}i_C - \frac{R + R_s}{\ell_s}i_s - \frac{R}{\ell_s}i_o. \tag{20e}$$

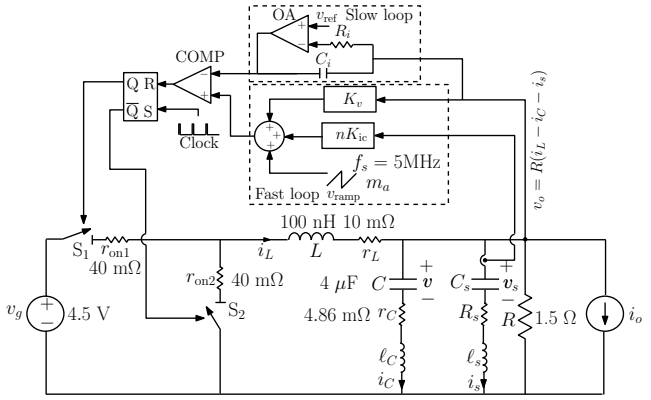


Fig. 10. A buck converter under a ripple-based $\mathrm{V^2I}_C$ control scheme corresponding to Example 5. The parameter values used for this example are also shown. The rest of parameter values not indicated in the figure are shown in the text.

Accordingly, the system matrices and vectors are:

$$\mathbf{A}_1 = \begin{pmatrix} 0 & 0 & 0 & \frac{1}{C} & 0 \\ 0 & 0 & 0 & 0 & \frac{1}{C_s} \\ 0 & 0 & -\frac{R_1}{L} & \frac{R}{L} & \frac{R}{L} \\ \frac{1}{\ell_C} & 0 & \frac{R}{\ell_C} & -\frac{R+r_C}{\ell_C} & -\frac{R}{\ell_C} \\ 0 & -\frac{1}{\ell_s} & \frac{R}{Ls} & -\frac{R}{\ell_s} & -\frac{R+Rs}{\ell_s} \end{pmatrix}, \tag{21a}$$

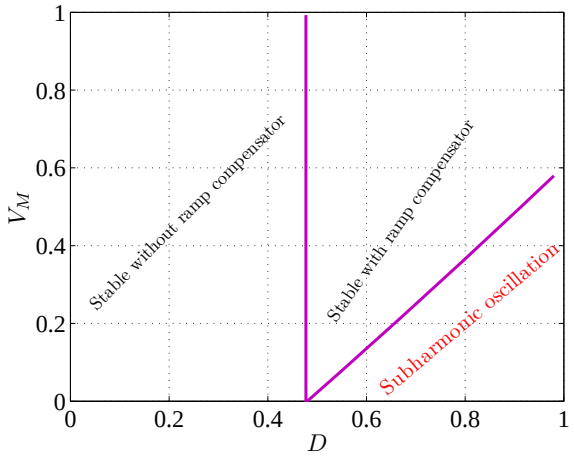
$$\mathbf{A}_0 = \begin{pmatrix} 0 & 0 & 0 & \frac{1}{C} & 0 \\ 0 & 0 & 0 & 0 & \frac{1}{C_s} \\ 0 & 0 & -\frac{R_2}{L} & \frac{R}{L} & \frac{R}{L} \\ -\frac{1}{\ell_C} & 0 & \frac{R}{\ell_C} & -\frac{R+r_C}{\ell_C} & -\frac{R}{\ell_C} \\ 0 & -\frac{1}{\ell_s} & \frac{R}{\ell_s} & -\frac{R}{\ell_s} & -\frac{R+Rs}{\ell_s} \end{pmatrix}, \tag{21b}$$

$$\mathbf{B}_1 = \begin{pmatrix} 0 & 0 \\ 0 & 0 \\ \frac{1}{L} & \frac{R}{L} \\ 0 & 0 \\ 0 & 0 \end{pmatrix}, \ \mathbf{B}_0 = \begin{pmatrix} 0 & 0 \\ 0 & 0 \\ 0 & \frac{R}{L} \\ 0 & 0 \\ 0 & 0 \end{pmatrix}. \tag{21c}$$

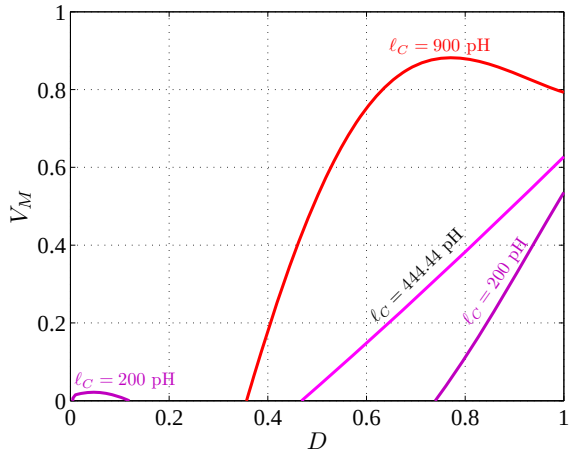
The feedback vector $\mathbf{K}$ and the input vector $\mathbf{w}$ are as follows:

$$\mathbf{K} = \begin{pmatrix} 0 \\ 0 \\ K_v R \\ -K_v R \\ nK_{ic} - K_v R \end{pmatrix}, \ \mathbf{w} = \begin{pmatrix} v_g \\ i_o \end{pmatrix}. \tag{22}$$

The system was recently studied in [18] from a nonlinear dynamics perspective using Floquet theory and discrete-time-modeling approaches. The critical compensator slope for stability was obtained using numerical simulations from the switched model and validated by checking when one of the eigenvalues of the monodromy matrix becomes -1. The results were also validated experimentally. For comparison, stability boundaries presented in [18] are plotted in Fig. 11 using (2). Corrected parameter values taken from [20][3] that are slightly different from the ones reported in [18] were used. A good agreement can be observed by comparing Fig. 11 here and Fig. 16 in [18].



(a)

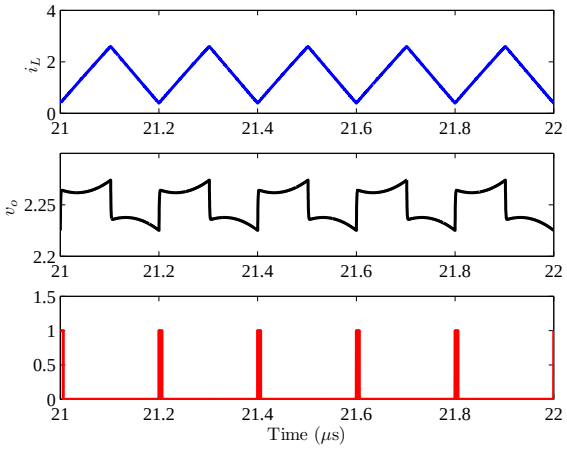


(b)

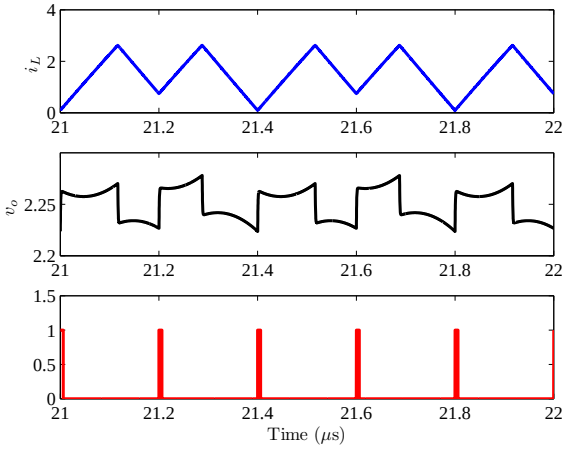
Fig. 11. Subharmonic oscillation curves in terms of the steady-state duty cycle D and the ramp amplitude $V_M = m_a T$ for a buck converter under a ripple-based $\mathrm{V^2I}_C$ control scheme and considering parasitic components (a) for ESL $\ell_C = 400$ pH indicating the stable and the subharmonic oscillation regions, (b) for different values of ESL ℓ_C.

Numerical simulations using PSIM© were used to confirm the theoretical results corresponding to this Example. The results are shown in Fig. 12. Let $V_M = 0.6$ V and $D = 0.5$ ($v_{\rm ref} = 2.25$ V), the converter is stable as predicted in Fig. 11 and confirmed by numerical simulations from the switched circuit-level model depicted in Fig. 12(a). Let $V_M = 0.5$ V and $D = 0.5$, the converter exhibits subharmonic oscillation as pre-

[3]The first author of [18] was contacted by a private communication via email regarding Fig. 16 in [18] and he was gracious to revise the parameter values and to provide correct data that were actually used to produce Fig. 16 in [18]. He recalled that the correct parameter values are the ones appearing in [21] not in [18].

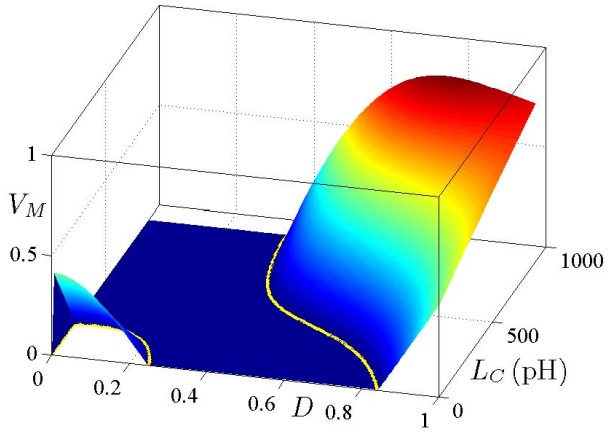


(a) $V_M = 0.6$ V

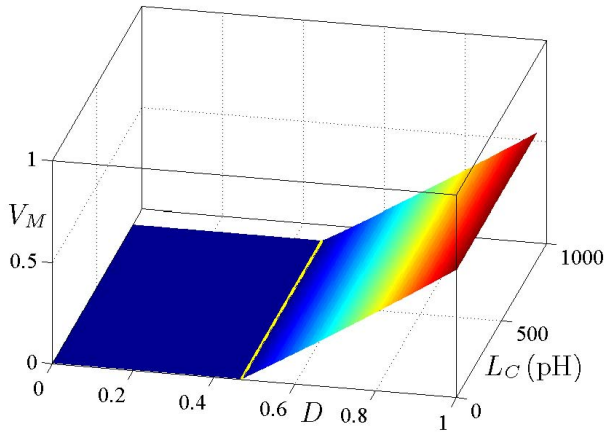


(b) $V_M = 0.5$ V

Fig. 12. Waveforms of the buck converter under a ripple-based V^2I_C control scheme for different values of ramp amplitudes V_M. Other parameters are: $\ell_c = 900$ pH, ℓ_s=400 pH.



(a) $\ell_s = 444.44$ pH



(b) $\ell_s = 1000L_C$ V

Fig. 13. Stability boundary of the buck converter under V^2I_C control showing the effect of the ESL L_C on the stability boundary for perfectly matched and non matched current sensor.

dicted in Fig. 11 and confirmed by the numerical simulations shown in Fig. 12(b). Note that the output voltage ripple of this converter is discontinuous at the switching instants because it is dominated by the ESL of the output capacitor. However even with this discontinuity, the integral term $W_i e(DT)$ was checked to have a negligible effect on the stability limit of the system since the voltage ripple is maintained at a very low level (1%). It should be noted that according to [18] when the current sensor is not perfectly matched and L_c decreases, the stability range is widened and the system is stable for all values of the steady-state duty cycle D smaller than a critical value close to 0.5. However, it can be observed in Fig. 12 that a small instability region, not detected in [18], appears in this case for small values of D. Fig. 13 shows a mesh plot representing the stability boundary for two difference cases. This boundary for the matched case is very similar to CMC and the critical value D_c of the duty cycle is close to 0.5 without ramp compensation ($V_M = 0$) regardless of the value of L_C while in the non matched case, there is a strong dependence of the critical duty cycle D_c on L_C. In this case, for relatively small values of L_C, and without ramp compensation, $V_M = 0$, the stability is guaranteed only within a certain window of the steady-state duty cycle D (Fig. 13(a)). This is not the case when L_c and ℓ_s are matched for which if the stability is guaranteed for a certain value of the duty cycle D_c, it will be also guaranteed for all values of D smaller than D_c (Fig. 13(b)).

C. Example 5: A buck converter under a type-III VMC scheme and loaded by a current sink [22]

Consider the buck converter under a type-III VMC scheme loaded by a current sink i_o studied in [22]. Fig. 14 shows the circuit diagram and the fixed parameter values. The transfer function of the controller can be expressed as follows:

$$H_v(s) = \frac{W_i}{s}\frac{(1+s/\omega_{z1})(1+s/\omega_{z2})}{(1+s/\omega_{p1})(1+s/\omega_{p2})}. \quad (23)$$

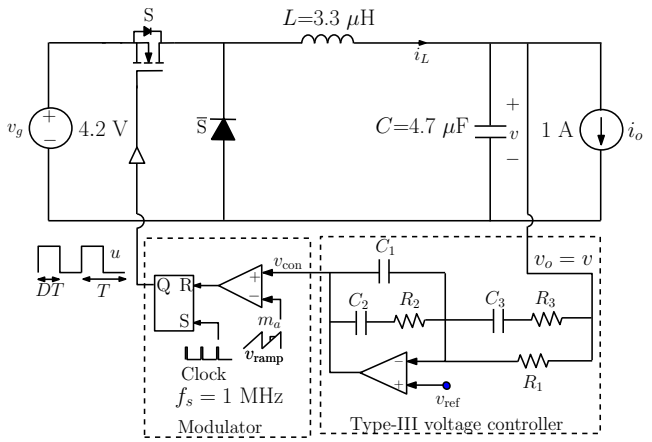


Fig. 14. A buck converter under a type-III VMC scheme loaded by a current sink of Example 5 [22].

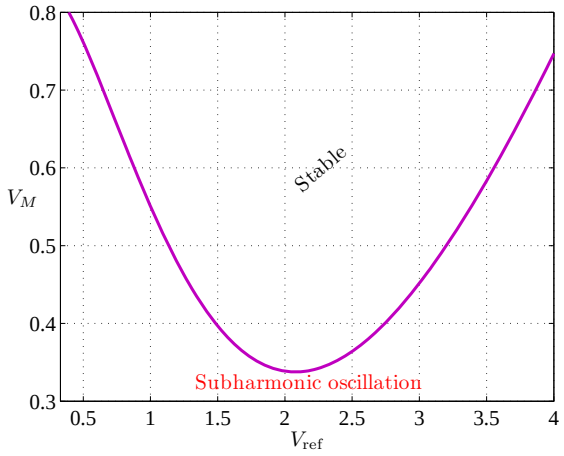


Fig. 15. Subharmonic oscillation boundary in terms of the output voltage reference $V_{\rm ref}$ and the ramp amplitude $V_M = m_a T$ for a buck converter under a type-III VMC and loaded with a current sink [22].

The zeros, the poles and the integrator gain are given by the following expressions in terms of the passive components:

$$\begin{aligned} \omega_{z1} &= \frac{1}{R_2C_2},\ \omega_{z2} = \frac{1}{(R_1+R_3)C_3}, \omega_{p1} = \frac{C_1+C_2}{R_2C_1C_2}, \\ \omega_{p2} &= \frac{1}{R_3C_3},\ W_i = \frac{1}{R_1(C_1+C_2)}. \end{aligned} \tag{24}$$

Similar to Example 3, for this ideal buck converter one has $v_{\rm ref} = Dv_g$ in steady-state. The state equations are given by:

$$\frac{{\rm d}v}{{\rm d}t} = \frac{i_L}{C} - \frac{i_o}{C} \tag{25a}$$

$$\frac{{\rm d}i_L}{{\rm d}t} = -\frac{v}{L} + \frac{v_g}{L}u \tag{25b}$$

$$\frac{{\rm d}v_{p1}}{{\rm d}t} = -\omega_{p1}v_{p1} + v_{\rm ref} - v \tag{25c}$$

$$\frac{{\rm d}v_{p2}}{{\rm d}t} = -\omega_{p2}v_{p2} + v_{\rm ref} - v \tag{25d}$$

where v_{p1} and v_{p2} are the state variables due to the voltage controller. As detailed in Example 2 in Part I, the control signal in the case of a type-III controller can be expressed as $v_{\rm con} = W_{p1}v_{p1} + W_{p2}v_{p2} + W_i x_i$, where W_i is the integrator gain, x_i being the integral of the voltage error and W_{p1} and W_{p2} are feedback coefficient corresponding to the state variables v_{p1} and v_{p2} that can be expressed as follows:

$$W_{p1} = \frac{W_i\omega_{p2}(\omega_{z1}\omega_{z2} - \omega_{p1}(\omega_{z1}+\omega_{z2}) + \omega_{p1}^2)}{\omega_{z1}\omega_{z2}(\omega_{p1}-\omega_{p2})}, \tag{26a}$$

$$W_{p2} = -\frac{W_i\omega_{p1}(\omega_{z1}\omega_{z2} - \omega_{p2}(\omega_{z1}+\omega_{z2}) + \omega_{p2}^2)}{\omega_{z1}\omega_{z2}(\omega_{p1}-\omega_{p2})}, \tag{26b}$$

which, as explained in Part I, can be obtained by performing a partial fraction decomposition (See Example 2 in Part I). With the selected state variables, the state-space system matrices and vectors are as follows:

$$\mathbf{A}_1 = \mathbf{A}_0 = \begin{pmatrix} 0 & \frac{1}{C} & 0 & 0 \\ -\frac{1}{L} & 0 & 0 & 0 \\ -1 & 0 & -\omega_{p1} & 0 \\ -1 & 0 & 0 & -\omega_{p2} \end{pmatrix}, \tag{27a}$$

$$\mathbf{B}_1 = \begin{pmatrix} -\frac{1}{C} & 0 & 0 \\ 0 & \frac{1}{L} & 0 \\ 0 & 0 & 1 \\ 0 & 0 & 1 \end{pmatrix}, \mathbf{B}_0 = \begin{pmatrix} -\frac{1}{C} & 0 & 0 \\ 0 & 0 & 0 \\ 0 & 0 & 1 \\ 0 & 0 & 1 \end{pmatrix} \tag{27b}$$

The feedback vector $\mathbf{K}$ and the input vector $\mathbf{w}$ are given by:

$$\mathbf{K} = \begin{pmatrix} 0 \\ 0 \\ -W_{p1} \\ -W_{p2} \end{pmatrix}, \ \mathbf{w} = \begin{pmatrix} i_o \\ v_g \\ v_{\rm ref} \end{pmatrix}. \tag{28}$$

In [22] the stability boundary was determined in the parameter space $(V_{\rm ref}, V_M)$, $V_M = m_a T$, using a circuit-oriented geometrical approach and the results were validated by an accurate SPICE-level circuit simulator. The same stability boundary is reproduced here using the same parameter values for comparison. In particular, the controller parameters are as follows: $\omega_{z1} = 0.167$ Mrad/s, $\omega_{z2} = 0.33$ Mrad/s, $\omega_{p1} = 5$ Mrad/s, $\omega_{p2} = 7$ Mrad/s. Other parameter values are shown in Fig. 14. Fig. 15 shows the stability boundary plotted by using (2). A perfect agreement can be observed between the results in Fig. 15 here and those in Fig. 6 in [22]. It has also been checked that if the integral term $W_i e(DT)$ is removed from (2), the stability curve barely changes. Hence, like in all VMC strategies, the integral term is also negligible for this example and can be ignored because $v_{\rm ref} - v_o(DT) = v_{\rm ref} - v(DT) \approx 0$.

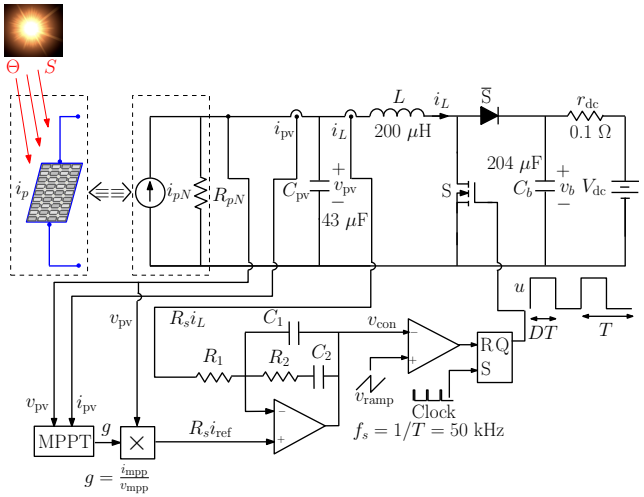


Fig. 16. A boost converter fed by a PV source with input feedback for PV applications (Example 6).

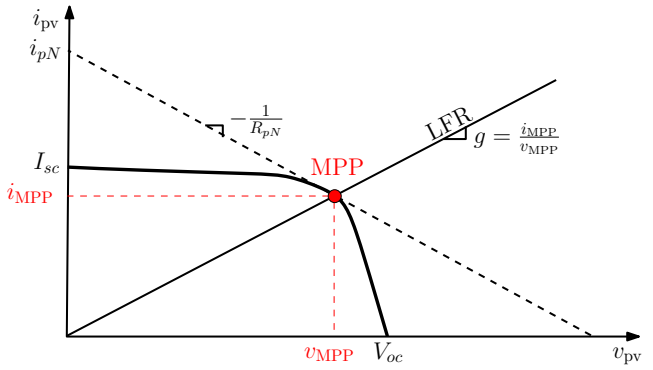


Fig. 17. PV curve and its linear representation at the MPP together with the load line of an ideal LFR.

IV. Additional Practical Example with Experimental Validation

Since most of the results in the previous sections were already verified with extensive simulation and experimental results in previous studies, there is no point of repeating the efforts. However, a boost converter for PV applications is considered in this section. Its experimental prototype were implemented and several experimental tests were performed.

A. Example 6: An input controlled boost converter for PV applications

Consider a boost converter fed by a PV source and loaded by a constant voltage source for PV systems. As the solar irradiation G or the temperature Θ change during the operation, the voltage/current of the PV array is adjusted to correspond to the maximum available power. In this paper, the input voltage $v_{\rm pv}$ and the inductor current i_L of the system are controlled to be proportional ($i_L = g v_{\rm pv}$) in such a way to impose a fixed frequency loss free resistor (LFR) [27], where $g = i_{\rm mpp}/v_{\rm mpp}$ is provided by the maximum power point tracking (MPPT) controller which forces the system to operate at the MPP of the PV array regardless the weather conditions. Fig. 16 shows the circuit diagram of the system under input voltage and inductor current feedback by imposing an LFR behavior. In this kind of applications, the input must be controlled [23]–[26] while the output voltage is fixed by appropriate means. For instance, the battery symbol in Fig. 16 implies a dc bus whose voltage is relatively constant and can also represent a storage device like a battery or a super capacitor. It can also represent a dc link voltage regulated by a grid-connected inverter. The input current source i_{pN} and the resistance R_{pN} correspond to the Norton equivalent current and impedance at the MPP (Fig. 17). In order to obtain these two parameters, the nonlinear model of the PV source must be linearized in the vicinity of the MPP where the system is supposed to work. One of the most widely used models for a PV panel is the single diode model, which, in many applications, represents a good compromise between accuracy and simplicity. The equation of the single diode model can be written as follows [28]:

$$i_{\rm pv} = I_{\rm pv} - I_s \left(e^{\dfrac{v_{\rm pv} + r_s i_{\rm pv}}{V_{\rm ta}}} - 1 \right) - \frac{v_{\rm pv} + r_s i_{\rm pv}}{R_p}, \quad (29)$$

where $v_{\rm pv}$ is the voltage of the module, $I_{\rm pv}$ and I_s are the photogenerated and saturation currents respectively, $V_{\rm ta}$ is the thermal voltage which is given by $V_{\rm ta} = N_s A K \theta / q$ where A is the diode quality factor, K is Boltzmann constant, q is the charge of the electron, Θ is the PV module temperature and N_s is the number of the cells connected in series. The photogenerated current $I_{\rm pv}$ depends on the irradiance G and temperature Θ according to the following equation:

$$I_{\rm pv} = I_{\rm sc} \frac{G}{G_n} + C_\Theta (\Theta - \Theta_n), \quad (30)$$

being $I_{\rm sc}$ the short circuit current, Θ_n and G_n the nominal temperature and irradiance respectively and C_Θ the temperature coefficient. Practical PV generators have a series resistance r_s and a parallel resistance R_p although they can be ignored for simplicity purposes. Close to the MPP, the PV source can be linearized by expanding the PV nonlinear model as a Taylor series and ignoring high-order terms hence obtaining (see Fig. 17):

$$i_{\rm pv} \approx i_{\rm mpp} - \frac{1}{R_{pN}} (v_{\rm pv} - v_{\rm mpp}). \quad (31)$$

Therefore, the equivalent Norton current i_{pN} is given by:

$$i_{pN} = i_{\rm mpp} + \frac{v_{\rm mpp}}{R_{pN}}, \quad (32)$$

and by using the implicit function theorem, the equivalent Norton resistance R_{pN} near the MPP can be expressed as follows:

$$R_{pN} = \frac{(r_s + R_p) V_{\rm ta} + r_s R_p I_s e^{\frac{v_{\rm mpp} + r_s i_{\rm mpp}}{V_{\rm ta}}}}{R_p I_s e^{\frac{v_{\rm mpp} + r_s i_{\rm mpp}}{V_{\rm ta}}} + V_{\rm ta}}. \quad (33)$$

Hence, by applying Kirchhoff's voltage and current laws to the circuit depicted in Fig. 16, the following set of differential equations describing the power stage is obtained:

$$\frac{\mathrm{d}v_{\mathrm{pv}}}{\mathrm{d}t} = \frac{i_{pN}}{C_{\mathrm{pv}}} - \frac{v_{\mathrm{pv}}}{C_{\mathrm{pv}}R_{pN}} - \frac{i_L}{C_{\mathrm{pv}}}, \quad (34a)$$

$$\frac{\mathrm{d}i_L}{\mathrm{d}t} = \frac{v_p}{L} - \frac{V_{\mathrm{dc}}}{L}(1-u), \quad (34b)$$

$$\frac{\mathrm{d}v_b}{\mathrm{d}t} = \frac{i_L}{C_b}(1-u) + \frac{V_{\mathrm{dc}} - v_b}{r_{\mathrm{dc}}C_b}. \quad (34c)$$

A type-II controller is used to impose the LFR behavior. Its transfer function can be expressed as follows:

$$H_i(s) = \frac{W_i}{s}\frac{(1+s/\omega_z)}{(1+s/\omega_p)}. \quad (35)$$

where W_i is the integrator gain. The zeros, the poles and the integrator gain are given by the following expressions in terms of the passive components:

$$\omega_z = \frac{1}{R_2C_2},\ \omega_p = \frac{1}{R_2C_{12}},\ W_i = \frac{1}{R_1(C_1+C_2)}. \quad (36)$$

where $C_{12} = C_1C_2/(C_1+C_2)$. Performing a partial fraction decomposition, the transfer function in (35) becomes:

$$H_i(s) = \frac{W_i}{s} + \frac{W_p}{s+\omega_p}, \quad (37)$$

where W_p is given by the following expression:

$$W_p = \frac{W_i}{\omega_z}(\omega_p - \omega_z). \quad (38)$$

Using (37), the state equation corresponding to the state variable v_p of the controller can be expressed as follows:

$$\frac{\mathrm{d}v_p}{\mathrm{d}t} = -\omega_p v_p + (i_L - g v_{\mathrm{pv}}). \quad (39)$$

Let the state vector be $\mathbf{x} = (v_{\mathrm{pv}},\ i_L\ , v_b\ , v_p)^{\intercal}$. Accordingly, the system matrices and vectors are given by:

$$\mathbf{A}_1 = \begin{pmatrix} -\frac{1}{R_{pN}C_p} & -\frac{1}{C_p} & 0 & 0 \\ \frac{1}{L} & -\frac{r_L+r_C}{L} & 0 & 0 \\ 0 & 0 & -\frac{1}{r_{\mathrm{dc}}C} & 0 \\ -g & 1 & 0 & -\omega_p \end{pmatrix}, \quad (40a)$$

$$\mathbf{A}_0 = \begin{pmatrix} -\frac{1}{R_{pN}C_p} & -\frac{1}{C_p} & 0 & 0 \\ \frac{1}{L} & -\frac{r_L+r_C}{L} & 0 & 0 \\ \frac{1}{L} & 0 & -\frac{1}{r_{\mathrm{dc}}C} & 0 \\ -g & 1 & 0 & -\omega_p \end{pmatrix}, \quad (40b)$$

$$\mathbf{B}_1 = \begin{pmatrix} \frac{1}{C} & 0 \\ 0 & 0 \\ 0 & \frac{1}{r_{\mathrm{dc}}C} \\ 0 & 0 \end{pmatrix},\ \mathbf{B}_0 = \begin{pmatrix} \frac{1}{C} & 0 \\ 0 & -\frac{1}{L} \\ 0 & \frac{1}{r_{\mathrm{dc}}C} \\ 0 & 0 \end{pmatrix}. \quad (40c)$$

For this example, the feedback vector $\mathbf{K}$ and the input vector $\mathbf{w}$ are as follows:

$$\mathbf{K} = \begin{pmatrix} 0 \\ 0 \\ 0 \\ W_p \end{pmatrix},\ \mathbf{w} = \begin{pmatrix} i_{pN} \\ V_{\mathrm{dc}} \end{pmatrix}. \quad (41)$$

The steady-state duty cycle D is related to the average value of the PV source voltage V_{pv} and the dc output voltage V_{dc} as follows:

$$D = \frac{V_{\mathrm{dc}} - V_{\mathrm{pv}}}{V_{\mathrm{dc}}}, \quad (42)$$

which can be obtained by performing a net volt-second balance in steady-state regime.

B. Experimental setup

The experimental setup used for obtaining the experimental results is depicted in Fig. 18 where the boost converter, its control broad, the load, the power sources and signal generators can be identified. The inductor was built using toroidal Magnetics Kool-mu© and its inductance value is 200 μH. The output capacitor is the parallel connection of five metallized polyester (MKT) capacitors each has a capacitance of 10 μF and seventy ceramic (X7R) capacitors each has a capacitance of 2.2 μF. The total capacitance is 204 μF. The input capacitor is the parallel connection of one metallized polyester (MKT) capacitor with a capacitance value of 10 μF and fifteen ceramic (X7R) capacitors each with a capacitance value of 2.2 μF. The total input capacitance is 43 μF. The switch used is an IRFP4110PBF Silicon MOSFET and the diode is an MBR30H100CTG Silicon Schottky diode. The rated voltage of all the capacitors, switch and diode is 100 V. The inductor current sensing was carried out by an LA25-NP Hall effect current transducer. A PV emulator AGILENT E4361A was used as a PV source allowing to obtain repeatable experiments. The emulator was set with an open circuit voltage $V_{\mathrm{oc}} = 22.1$ V, an MPP voltage $v_{\mathrm{mpp}} \approx 18.17$ V, a short circuit current $I_{\mathrm{sc}} \approx 5$ A and an MPP current $i_{\mathrm{mpp}} = 4.68$ A. In order to emulate an ideal constant voltage sink at the converter output, an electronic load (ELEKTRO-AUTOMATIK EL3400-25) was used. The steady-state duty cycle was varied by adjusting the load voltage. To obtain the LFR behavior, a current reference was generated by multiplying, using an analog multiplier (AD633JNZ), the PV panel voltage by a signal from a generator (Tektronix AFG2021) which emulates the conductance g selected to be equal to $g_{\mathrm{mpp}} = i_{\mathrm{mpp}}/v_{\mathrm{mpp}} = 0.2575$ S. Subtracting the inductor current from the generated reference, the error is obtained which is then processed by a PI controller with a variable proportional gain. The controller output is low pass filtered using a 25 kHz cut-off frequency, which is one half the switching frequency. Note that this configuration, consisting of a PI controller cascaded with a low pass filter, is equivalent to a type-II controller. The output of this filter is compared with a 50 kHz sawtooth ramp signal provided from another signal generator (Tektronix AFG2021). When the ramp signal is larger than the control signal, the comparator LM319N forces the SR flip-flop CD4027BE to reset, and the driving

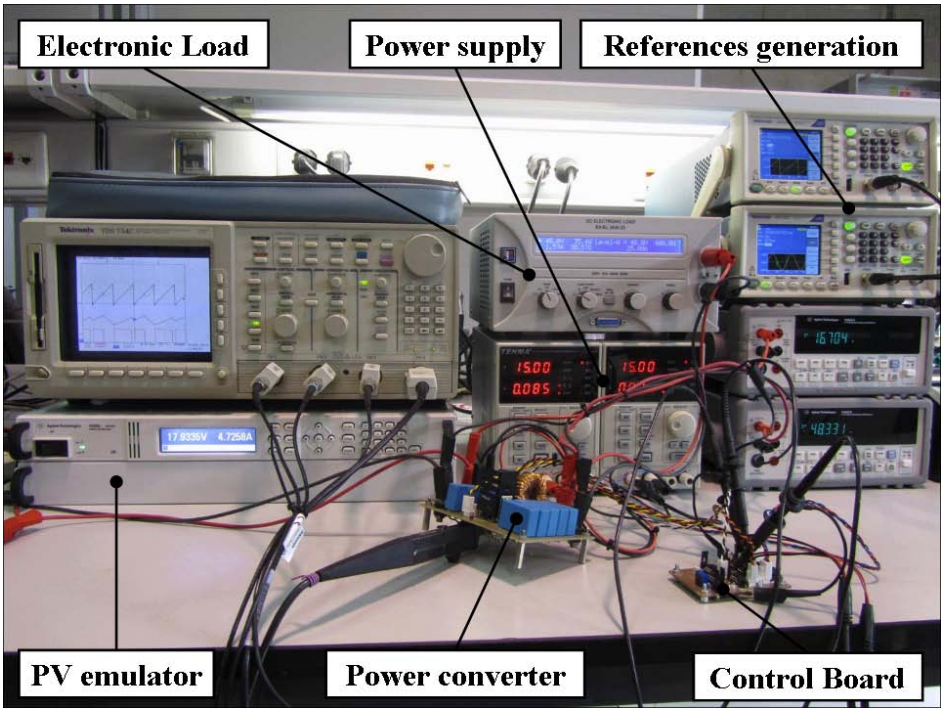


Fig. 18. The experimental setup used to validate the theoretical and the simulation results.

signal will be zero. At the end of each period of the ramp, another comparator LM3l9N forces a set for the SR flip-flop, placing the driving signal to 1. The output of the SR flip-flop is the switch driving signal by means of the driver MCP1407-E/P. The results, shown below, were measured by using the oscilloscope Tektronix TDS 754C and the probes TEKTRONIX TCP202 for illustrating the current waveforms.

C. Results and discussions

In order to apply the closed-form expression given in (2) to this system, an automated procedure was used to detect the MPP, linearize the PV source in its vicinity and to obtain the optimum value of g corresponding to the MPP as explained in the previous section. Once the parameters g, R_{pN} and i_{pN} of the system are obtained, expression (2) can be readily applied as in the previous examples. The stability boundary of the system is plotted in Fig. 19 in terms of different parameters. The fixed parameter values are the same ones described in the previous section. The plot in Fig. 19(a)-(b) was obtained by using expression (2) and experimentally. A remarkable agreement can be observed between the results which show that the first instability that takes place in the system $T-$periodic orbit when the parameter W_p is varied is a period-doubling leading to subharmonic oscillation. Time domain waveforms of the inductor current and the control signals are shown in Fig. 20 just before and just after subharmonic oscillation is exhibited. The results are obtained experimentally using the nonlinear PV emulator source. Similar results have been also obtained from numerical simulations of the circuit-level switched model.

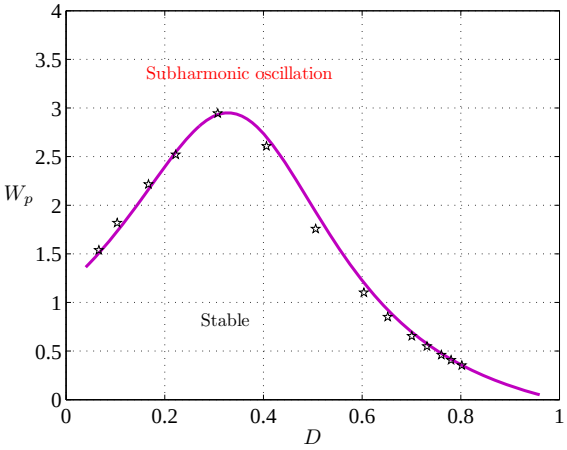
Finally, it is worth noting that the approach presented in the present work was also applied to many other examples dealing with nonlinear dynamics in switching regulators such as [12], [13], [16], [29]–[34]. In all the cases the agreement was perfect in predicting the onset of subharmonic oscillation. It is also worth noting that many complex power electronics systems can be approximated by a switched model with two configurations and the approach presented in this paper can also be applied to this kind of systems. This is the case, for instance, of [35], [36].

ACKNOWLEDGMENTS

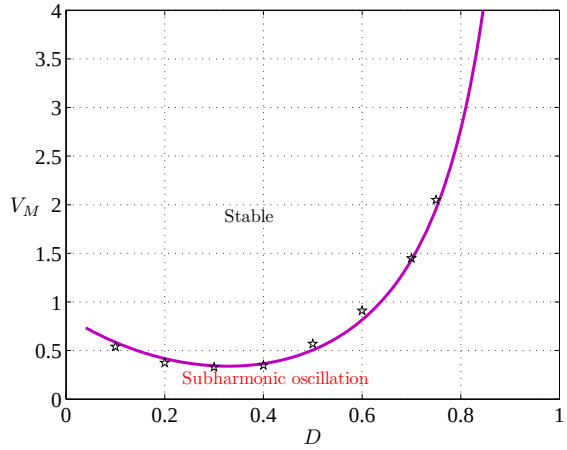
The author would like to thank the anonymous reviewers for their valuable comments and suggestions to improve the readability of Part I and Part II of this work. He also would like to express his thanks to Dr. J. M. Bosque-Moncusi, from the GAEI research center, Departament d'Enginyeria Electrònica, Elèctrica i Automàtica, Escola Tècnica Superior d'Enginyeria, Universitat Rovira i Virgili, SPAIN, for his assistance in getting the experimental results.

V. CONCLUSIONS

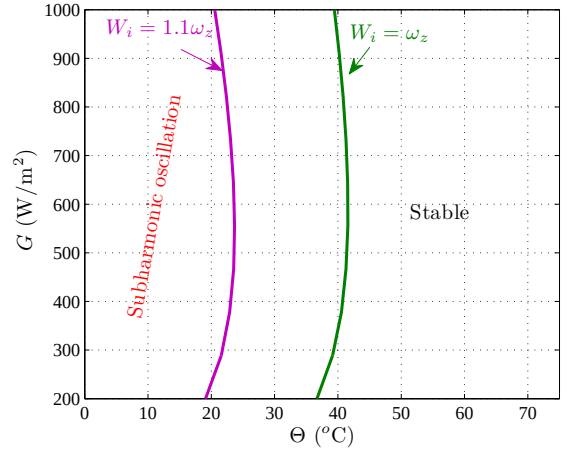
Part I of this work presented a novel approach for deriving the subharmonic oscillation boundary in switching regulators. In this paper, the usefulness of the approach proposed in Part I was illustrated clearly via six case-studies. The different examples showed that the new derived expression accurately predicts subharmonic oscillation occurrence in switching converters under different fixed frequency control strategies. Although, a priori, the approach can only be applied to switching converters with linear configurations for each switch state, a procedure was presented to deal with switching converters with nonlinear sources such as PV arrays or fuel cells. This approach offers therefore a valuable guidance in assessing the stability of the system, particularly as nonlinearity and/or



(a)

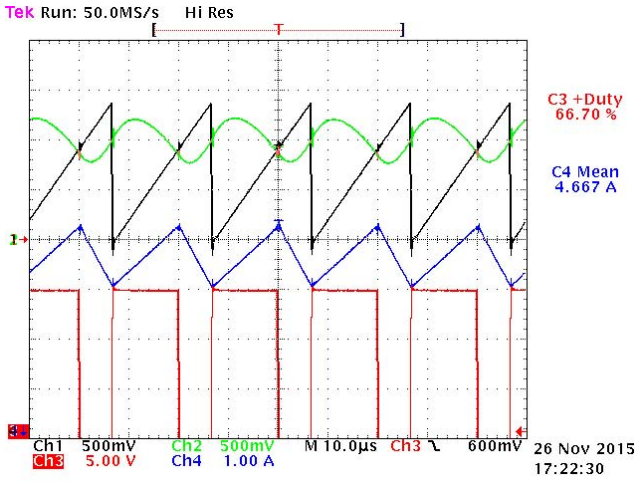


(b)

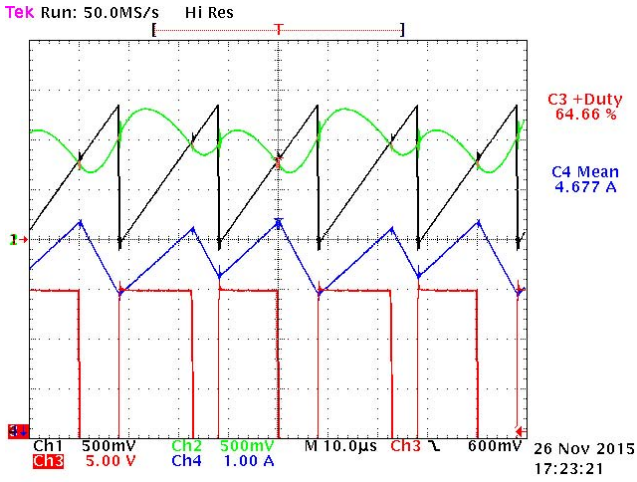


(c)

Fig. 19. The stability boundary from theoretical analysis using (2) and experimentally ($\star$). (a) in terms of the gain W_p and the steady-state duty cycle D. (b) in terms of the ramp amplitude V_M and the steady-state duty cycle D, (c) in terms of the temperature Θ and the irradiance G. $\omega_p = 25$ krad/s. $\omega_z = 1$ krad/s. V_M =1 V. The stable region is at the left of the curves.



(a) $V_M = 1.35$ V



(b) $V_M = 1.3$ V

Fig. 20. Experimental waveforms of PV-fed the boost converter with input variables control before (a) and after (b) subharmonic oscillation takes place. $V_{\text{bat}} = 55$ V ($D = 0.67$).

uncertainty in renewable generation can be taken into account. It was shown that the new analytical expression can be particularly useful in showing the dependance of the stability boundary on the system parameters. For design-oriented prediction of subharmonic oscillation, approximating the exact expression is desirable, with [37] offering an appealing approach. Namely, by truncating the exponential matrix series up to a specified order depending on the converter topology and the control strategy, simplified design-oriented expressions can be derived that can be interpreted in terms of the slope or the ripple of the control signal relative to that of the external ramp signal [37]. The new derived approach may also offer a framework for systematically evaluating the subharmonic oscillation boundary of more complex structures. Further work is required, though, to apply the approach for switching converters working under discontinuous conduction mode as well as for larger networks with multiple switching configurations.

APPENDIX: MATLAB©CODE FOR PLOTTING SUBHARMONIC OSCILLATION BOUNDARY

```
%%%% Prepared by A. El Aroudi on May 28th 2016 %%%%
%This code can be used for plotting subharmonic
%oscillation boundary in switching %converters with
%fixed frequency control and it can also adapted for
%Saddle-Node instability boundaries.

close all, clear all, clc,
%Introduce plant and controller parameter values.
vg=4.2; L=3.3e-6; C=4.7e-6; T=1/1e6;wz1=0.167e6;
wz2=0.33e6;wp1=5e6; wp2=7e6;Io=1;Wi=0.32e6;
% System feedback coefficients.
%This is the case of a type III compensator
Wp1 =  Wi*wp2*(wz1*wz2-wp1*wz1-wp1*wz2+wp1^2)/...
wz1/wz2/(wp1-wp2);
Wp2 = -Wi*wp1*(wz1*wz2-wp2*wz1-wp2*wz2+wp2^2)/...
wz1/wz2/(wp1-wp2);
% System state-space matrices.
   A1=[0 1/C  0 0;
       -1/L 0  0 0 ;
       -1 0 -wp1 0;
       -1 0  0 -wp2];
    A0=A1; % Only for an ideal buck converter.
           % Otherwise A0 must be introduced.
    B1=[-1/C 0 0;
         0 1/L 0;
         0 0 1;
         0 0 1];
    B0=[-1/C 0 0;
         0 0 0;
         0 0 1;
         0 0 1];
% Feedback vector and identity matrix.
K=[0 0 -Wp1 -Wp2]; II=eye(length(A1));
%Introduce steady-state duty cycle D range.
DD=linspace(0.0,1,200);
%Evaluating any dependence on D.
k=1; for D= DD;
vref=D*vg; % From net volt-second balance.
w=[Io; vg; vref]; % Input pàrameter vector
phi1=expm(A1*D*T); phi0=expm(A0*(1-D)*T);
psi1=inv(A1)*(phi1-eye(length(A1)))*B1*w;
% No singularity problem with the use
% of inv with the approach of this paper.

psi0=inv(A0)*(phi0-eye(length(A1)))*B0*w;
PHI=phi0*phi1; PSI=phi0*psi1+psi0;
x0=inv(eye(length(A1))-PHI)*PSI;
% No singularity problem with the use
% of inv with the approach of this paper
xD=phi1*x0+psi1; f1x0=A1*x0+B1*w;
f2x0=A0*x0+B0*w; evD=vref-xD(1);
mI=Wi*evD;
% Term due to the external integral variable
% It can be ignored without a significant error
% in all VMC strategies but not in CMC.
mP=-(K*inv(II+phi1*phi0)*phi1*(f1x0+f2x0));
PD(k)=mI+mP; k=k+1;
end
plot(DD*vg,PD*T,'m-','linewidth',2)
xlabel('vref'), ylabel('VM')
```

REFERENCES

[1] A. El Aroudi, "A new approach for accurate prediction of subharmonic oscillation in switching regulators–Part I: mathematical derivations," *IEEE Transactions on Power Electronics*, early access, doi: 10.1109/TPEL.2016.2606418, 2016.

[2] C. C.-Fang, "Critical conditions of saddle-node bifurcations in switching DC-DC converters," *International Journal of Electronics.* vol. 100, no. 8, pp. 1147-1174, 2013.

[3] A. El Aroudi, D. Giaouris, H. H. C. Iu and I. Hiskens, "A review on stability analysis methods for switching mode power converters," *IEEE Journal on Emerging Topics on Circuits and Systems,* vol.5, no.3, pp.302-315, 2015.

[4] E. Rodriguez, F. Guinjoan, A. El Aroudi, and E. Alarcon, "A ripple-based design-oriented approach for predicting fast-scale instability in dc-dc switching power supplies," IEEE Trans. Circuits Syst. I: Reg. Papers, vol. 59, no. 1, pp. 215-227, 2012.

[5] R. Gavagsaz-Ghoachani, M. Phattanasak, J.-P. Martin, S. Pierfederici, B. Davat, "Predicting the onset of bifurcation and stability study of a hybrid current controller for a boost converter,"*Mathematics and Computers in Simulation,* vol. 91, pp. 262-273, 2013.

[6] R. W. Erickson and D. Maksimovic, *Fundamentals of power electronics*, Lluwer, Springuer, 2001.

[7] M.-G. Kim, "Error amplifier design of peak current controlled (PCC) buck LED driver," *IEEE Transactions on Power Electronics,* vol. 29, no. 12, pp. 6789-6795, 2014.

[8] M.-G Kim, "Proportional-Integral (PI) compensator design of duty-cycle-controlled buck LED driver," *IEEE Transactions on Power Electronics,* vol. 30, no. 7, pp. 3852-3859, 2015.

[9] D. Giaouris, S. Maity, S. Banerjee, V. Pickert, and B. Zahawi, "Application of Filippov method for the analysis of subharmonic instability in DC-DC converters," *International Journal of Circuit Theory and Applications*, vol. 37, no. 8, pp. 899-919, 2009.

[10] D. Giaouris, S. Banerjee, B. Zahawi, V. Pickert, "Stability analysis of the continuous-conduction-mode buck converter via Filippov's method," *IEEE Transactions on Circuits and Systems I: Regular Papers,* vol. 55, no. 4, pp. 1084-1096, 2008.

[11] A. El Aroudi, E. Rodriguez, R. Leyva, E. Alarcon, "A design-oriented combined approach for bifurcation prediction in switched-mode power converters," *IEEE Transactions on in Circuits and Systems II: Express Briefs*, vol. 57, no. 3, pp. 218-222, 2010.

[12] J. H. B. Deane and D. C. Hamill, "Instability, subharmonics, and chaos in power electronic systems," *IEEE Transactions on Power Electronics,* vol. 5, no. 2, pp. 260-268, 1990.

[13] D. C. Hamill, J. H. B. Deane, and D. Jefferies, "Modeling of chaotic DC-DC converters by iterated nonlinear mappings," *IEEE Transactions on Power Electronics,* vol. 7, no. 1, pp. 25-36, 1992.

[14] E. Fossas and G. Olivar "Study of chaos in the buck converter," *IEEE Transactions on Circuits and Systems I: Fundamental Theory and Applications*, vol. 43, no. 1, pp. 13–25, 1996.

[15] M. di Bernardo, F. Vasca, "Discrete-time maps for the analysis of bifurcations and chaos in DC/DC converters," *IEEE Transactions on Circuits and Systems I: Fundamental Theory and Applications*, vol. 47, no. 2, pp. 130–143, 2000.

[16] A. El Aroudi, "Prediction of subharmonic oscillation in switching converters under different control strategies," *IEEE Transactions on Circuits and Systems II: Express Briefs*, vol. 62, no. 11, pp-910-914, 2014.

[17] Y. Chen, C. K. Tse, S. S. Qiu, L. Lindenmuller and W. Schwarz, "Coexisting fast-scale and slow-scale instability in current-mode controlled DC/DC converters: Analysis, simulation and experimental results," *IEEE Transactions on Circuits and Systems I: Regular Papers,* vol. 55, no. 10, pp. 3335-3348, 2008.

[18] J. Cortes, V. Svikovic, P. Alou, J. A. Oliver, J. A. Cobos, R. Wisniewski, "Accurate analysis of subharmonic oscillations of V^2 and $V^2 I_c$ controls applied to buck converter," *IEEE Transactions on Power Electronics,* vol. 30, no. 2, pp. 1005-1018, 2015.

[19] S. Kapat, S., P. T. Krein, "Formulation of PID control for DC-DC converters based on capacitor current: A geometric context," *IEEE Transactions on Power Electronics,* vol. 27, no. 3, pp. 1424-1432, 2012.

[20] J. Cortes, Personal email commnuncation taken place on November, 9th 2015.

[21] J. Cortes, V Svikovic, P Alou, J Oliver, J Cobos, "Design and analysis of ripple-based controllers for buck converters based on discrete modeling and Floquet theory," IEEE 14th Workshop Control and Modeling for Power Electronics (COMPEL), 2013.

[22] L. Cheng, W.-H. Ki,, "A circuit-oriented geometrical approach in predicting subharmonic oscillation of dc-dc converters with voltage-mode control," *IEEE International Symposium on Circuits and Systems,* ISCAS'2014, pp. 962-965, 1-5, 2014.

[23] E. Bianconi, J. Calvente, R. Giral, E. Mamarelis, G. Petrone, G. C. A. Ramos-Paja, G. Spagnuolo,M. Vitelli, M., "A fast current-based MPPT technique employing sliding Mode control," *IEEE Transactions on Industrial Electronics,* vol. 60, no. 3, pp. 1168-1178, 2012.

[24] W. Xiao; N. Ozog, W. G. Dunford, "Topology study of photovoltaic interface for maximum power point tracking," *IEEE Transactions on Industrial Electronics,* vol. 54, no. 3, pp. 1696-1704, 2007.

[25] W. Xiao; W. G. Dunford, P. R. Palmer, A. Capel, "Regulation of photovoltaic voltage," *IEEE Transactions on Industrial Electronics,* vol. 54, no. 3, pp. 1365-1374, 2007.

[26] J. Leppaaho, T. Suntio, "Characterizing the dynamics of the peak-current-mode-controlled buck-power-stage converter in photovoltaic applications," *IEEE Transactions on Power Electronics,* vol. 29, no. 7, pp. 3840-3847, 2014.

[27] A. Cid-Pastor, L. Martinez-Salamero, N. Parody, A. El Aroudi,"Analysis and design of a loss-free resistor based on a boost converter in PWM operation," *IEEE International Symposium on Circuits and Systems*, ISCAS2010, Paris, 2010.

[28] M. Villalva, J. Gazoli, and E. Filho, "Comprehensive approach to modeling and simulation of photovoltaic arrays," *IEEE Transactions on Power Electronics*, vol. 24, no. 5, pp. 1198–1208, 2009.

[29] C. K. Tse and W. C. Y. Chan, "Chaos from a current-programmed Cuk converter," *International Journal Circuit Theory and Applications,* vol. 23, no. 3, pp. 217-225, 1995.

[30] C. K. Tse, S. C. Fung, and M. W. Kwan, "Experimental confirmation of chaos in a current-programmed Čuk converter," *IEEE Transactions on Circuits and Systems I: Theory and Applications,* vol. 43, no. 7, pp. 605-608, 1996.

[31] S. K. Mazumder, A. H. Nayfeh, D. Boroyevich, "Theoretical and experimental investigation of the fast- and slow-scale instabilities of a DC-DC converter," *IEEE Transactions on Power Electronics,* vol. 16, no. 2, pp. 201-216, 2001.

[32] K. Chakrabarty, G. Poddar, and S. Banerjee, "Bifurcation behavior of the buck converter," *IEEE Transactions on Power Electronics,* vol. 11, no. 3, pp. 439-447, 1996.

[33] S. Banerjee and K. Chakrabarty, "Nonlinear modeling and bifurcation in the boost converter," *IEEE Transactions on Power Electronics,* vol. 13, no. 2, pp. 252-260, 1998.

[34] G. A. Papafotiou, N. I. Margaris, "Calculation and stability investigation of periodic steady states of the voltage controlled Buck DC-DC converter," *IEEE Transactions on Power Electronics,* vol. 19, no. 4, pp. 959-970, 2004.

[35] A. Shahin, R. Gavagsaz-Ghoachani, J.-P Martin, S. Pierfederici, Davat, B. F. Meibody-Tabar, "New method to filter HF current ripples generated by current-fed DC/DC converters," *IEEE Transactions on Power Electronics,* vol. 26, no. 12, pp. 3832-3842, 2011.

[36] R. Gavagsaz-Ghoachani, J.-P Martin, S. Pierfederici, B. Nahid-Mobarakeh, B. Davat, "DC power networks with very low capacitances for transportaion systems: dynamic behavior nalysis," *IEEE Transactions on Power Electronics,* vol. 28, no. 12, pp. 5865-5877, 2013.

[37] A. El Aroudi, M. Al-Numay, J. Calvente, R. Giral, E. Rodriguez and E. Alarcón, "Prediction of subharmonic oscillation in switching regulators: From a slope to a ripple standpoint," *International Journal of Electronics*, vol. 103, no. 12, pp. 2090-2109 , 2016.

[38] A. El Aroudi, "A Time-domain asymptotic approach to predict saddle-node and period doubling bifurcations in pulse width modulated piecewise linear systems," The *International Conference on Structural Nonlinear Dynamics and Diagnosis*, Agadir, Morocco, 2014.



Abdelali El Aroudi (M'00, SM'13) received the graduate degree in physical science from Facultt'e des sciences, Université Abdelmalek Essaadi, Tetouan, Morocco, in 1995, and the Ph.D. degree (hons) in applied physical science from Universitat Polit'ecnica de Catalunya, Barcelona, Spain in 2000. During the period 1999-2001 he was a Visiting Professor at the Department of Electronics, Electrical Engineering and Automatic Control, Technical School of Universitat Rovira i Virgili (URV), Tarragona, Spain, where he became an associate professor in 2001 and a full-time tenure Associate Professor in 2005. From September 2007 to January 2008 he was holding a visiting scholarship at the Department of Mathematics and Statistics, Universidad Nacional de Colombia, Manizales, conducting research on modeling of power Electronics circuits for energy management. From February 2008 to July 2008, he was a visiting scholar at the Centre de Recherche en Sciences et Technologies de Communications et de lt'Informations (CReSTIC), Reims, France. From September 2014 to December 2014, he was a visiting scholar at Institut National des Sciences Appliquées (INSA), Université of Toulouse, France and the Laboratoire d'Analyse et d'Architecture des Systèmes (LAAS) of the Centre National de la Recherche Scientifique (CNRS), Toulouse, France. From January 2015 to July 2015, he was a visiting professor at The Petroleum Institute, Abu Dhabi, UAE. His research interests are in the field of structure and control of power conditioning systems for autonomous systems, power factor correction, stability problems, nonlinear phenomena, chaotic dynamics, bifurcations and control. He is a Guest Editor of the IEEE Journal on Emerging and Selected Topics in Circuits and Systems Special Issue on Design of Energy-Efficient Distributed Power Generation Systems (September 2015). He currently serves as Associate Editor in *IEE IET Power Electronics* and *IEE IET Electronics Letters.*